Imaging and quantifying ganglion cells and other transparent neurons in the living human retina

Zhuolin Liu[a,1], Kazuhiro Kurokawa[a], Furu Zhang[a], John J. Lee[b], and Donald T. Miller[a]

[a]School of Optometry, Indiana University, Bloomington, IN 47405; and [b]Purdue School of Engineering and Technology, Indiana University–Purdue University Indianapolis, Indianapolis, IN 46202

Edited by David R. Williams, University of Rochester, Rochester, NY, and approved October 18, 2017 (received for review June 30, 2017)

Ganglion cells (GCs) are fundamental to retinal neural circuitry, processing photoreceptor signals for transmission to the brain via their axons. However, much remains unknown about their role in vision and their vulnerability to disease leading to blindness. A major bottleneck has been our inability to observe GCs and their degeneration in the living human eye. Despite two decades of development of optical technologies to image cells in the living human retina, GCs remain elusive due to their high optical translucency. Failure of conventional imaging—using predominately singly scattered light—to reveal GCs has led to a focus on multiply-scattered, fluorescence, two-photon, and phase imaging techniques to enhance GC contrast. Here, we show that singly scattered light actually carries substantial information that reveals GC somas, axons, and other retinal neurons and permits their quantitative analysis. We perform morphometry on GC layer somas, including projection of GCs onto photoreceptors and identification of the primary GC subtypes, even beneath nerve fibers. We obtained singly scattered images by: (*i*) marrying adaptive optics to optical coherence tomography to avoid optical blurring of the eye; (*ii*) performing 3D subcellular image registration to avoid motion blur; and (*iii*) using organelle motility inside somas as an intrinsic contrast agent. Moreover, through-focus imaging offers the potential to spatially map individual GCs to underlying amacrine, bipolar, horizontal, photoreceptor, and retinal pigment epithelium cells, thus exposing the anatomical substrate for neural processing of visual information. This imaging modality is also a tool for improving clinical diagnosis and assessing treatment of retinal disease.

adaptive optics | optical coherence tomography | organelle motility | retinal ganglion cells | retina

The retina is an inverted stack of neurons requiring light to traverse its full thickness before being absorbed by photoreceptors to initiate vision (1). Retinal neurons anterior to photoreceptors—including ganglion cells (GCs)—are therefore nearly transparent and well index matched to surrounding cells. These properties, combined with tight packing of the GCs, ocular blur, and retina motion, make these neurons extremely challenging to image in the living human eye (2–4). Ex vivo studies overcome these by removing the retina and using stains and fluorescent markers (5–7), two-photon excitation (8, 9), differential interference contrast optics (10), and extreme 3D resolution (11) to enhance contrast. Recently, some of these powerful methods have been applied successfully to animals in vivo as, for example, two-photon excitation (12), but work remains to translate them to human. However, standard methods of imaging the human retina in vivo—including fundus photography, scanning laser ophthalmoscopy (SLO), and optical coherence tomography (OCT)—fail to visualize GCs and the other transparent neurons due to insufficient resolution, axial sectioning, cell contrast, and correction of eye motion artifacts. Indirect methods of inferring neuron populations from bulk measures of retinal layer thicknesses and clinical visual field testing can circumvent these problems, but concerns about reliability remain (13).

Two recent advances in SLO have shown promise for observing GCs in the living human eye. One used SLO to detect apoptotic GCs tagged with an intravenously administered fluorescent marker (14), thus providing direct monitoring of GC loss. The second incorporated adaptive optics (AO)—which corrects ocular aberrations—into SLO sensitive to multiply-scattered light (12). This clever combination permitted imaging of a monolayer of GC layer (GCL) somas in areas with little or no overlying nerve fiber layer (NFL) (see figure 5, human result of Rossi et al.; ref. 12). By contrast, our approach uses singly scattered light and produces images of unprecedented clarity of translucent retinal tissue. This permits morphometry of GCL somas across the living human retina. We overcome the aforementioned obstacles by combining AO and OCT (AO-OCT) (15) to achieve high lateral and axial resolution and high sensitivity, using 3D subcellular image registration to correct eye motion, and using organelle motility inside GCL somas to increase cell contrast (16, 17). This imaging modality enables light microscopy of the living human retina, a tool for fundamental studies linking anatomical structure with visual function (18–21). High-resolution images of retinal neurons in living eyes also promise improved diagnosis and treatment monitoring of GC and axonal loss in diseases of the optic nerve such as glaucoma (3, 4, 22, 23) and other neurodegenerative disorders such as Alzheimer's disease, Parkinson's disease, and multiple sclerosis (24).

The 3D resolution of our AO-OCT method was $2.4 \times 2.4 \times 4.7\ \mu m^3$ (width × length × depth), sufficient to resolve GCL somas in any dimension. We acquired $1.5° \times 1.5°$ AO-OCT volume images along the horizontal meridian of the macula from four subjects free of ocular disease. AO-OCT videos were acquired at each retinal location with the system focused precisely at the GCL. In postprocessing, volumes were registered and averaged, and GCL somas were identified.

This report is based on a total count of over 42,000 GCL somas at 26 different locations in the four subjects. The 3D

Significance

Ganglion cells are the primary building block of retinal neural circuitry, but have been elusive to observe and quantify in the living human eye. Here, we show a light microscopy modality that reveals not only the somas of these cells, but also their 3D packing geometry, primary subtypes, and spatial projection to other neurons. The method provides a glimpse of the rich tapestry of neurons, glia, and blood vessels that compose the retina, thus exposing the anatomical substrate for neural processing of visual information. Clinically, high-resolution images of retinal neurons in living eyes hold promise for improved diagnosis and assessing treatment of ganglion cell and other neuron loss in retinal disease.

Author contributions: Z.L. and D.T.M. conceived and designed the project; Z.L., K.K., and J.J.L. developed image reconstruction, processing, and registration tools; Z.L. contributed new analytic tools, Z.L., K.K., and F.Z. performed the experiments, Z.L., K.K., F.Z., and D.T.M. analyzed the results; Z.L. and D.T.M. wrote the paper and all authors contributed to revisions; and D.T.M. supervised the project.

The authors declare no conflict of interest.

This article is a PNAS Direct Submission.

[1]To whom correspondence should be addressed. Email: liuzhuo@indiana.edu.

This article contains supporting information online at www.pnas.org/lookup/suppl/doi:10.1073/pnas.1711734114/-/DCSupplemental.

spatial coordinates of the GCL soma centers were marked and used to quantify: soma stack thickness, diameter, reflectance, density, and distribution of primary GC subtypes and GC projection onto cone photoreceptors (*Materials and Methods*).

Results and Discussion

Averaging and Registering AO-OCT Volumes. Imaging with coherent light produces speckle that contains both noise and object information (e.g., soma shape) (25), the former preventing observation of the latter (see example in Fig. 1; $n = 1$). Organelle motion in the soma causes the noise to change from image to image, while the object information (soma) remains constant from image to image, assuming the images are registered to each other with an accuracy better than the size of individual somas. Therefore, averaging of images reduces speckle noise while retaining soma information. We found empirically that averaging 100–160 registered AO-OCT volumes of the same retinal patch improved signal-to-noise ratio and image contrast, dramatically improving the clarity of individual GCL somas (see example in Fig. 1; $n = 137$). We quantified the image enhancement due to motion of organelles inside somas and our ability to register to subcellular accuracy using a soma contrast metric (*Materials and Methods*). As expected from the theory of independent noise realizations (25), soma contrast increased as the square root of the number of images averaged, experimentally increasing by a factor of 11 times with 137 volumes (Fig. 1 plot).

Three-Dimensional Imaging of the Inner Retina. Fig. 2 and corresponding Movie S1 illustrate the detailed views obtainable by our method of the 3D mosaic of GCL somas, the adjacent ganglion axon bundles, the retinal vasculature, and cellular structures at the inner limiting membrane (ILM) and inner plexiform layer (IPL). After imaging the retinal tissue at a selected location, the resulting volume can be dissected digitally to show how a single, identified neuron is positioned in depth (cross-sectional view, Fig. 2*C*) and laterally (transverse slice, Fig. 2*F*). Transverse slices provide detailed views of many retinal features of interest, such as presumptive astrocytes or microglia at the ILM (Fig. 2*D*), GC axon bundles of various calibers (Fig. 2*E*), the mosaic of GCL somas of different characteristic sizes indicating different functional classes (Fig. 2*F*), and the dense mesh of dendrites and synapses between GCs, amacrine cells, and bipolar cells in the IPL (Fig. 2*G*). Together, these images provide a glimpse of the rich tapestry of neurons, glia, and blood vessels that can be appreciated by interactive inspection of the imaged volume.

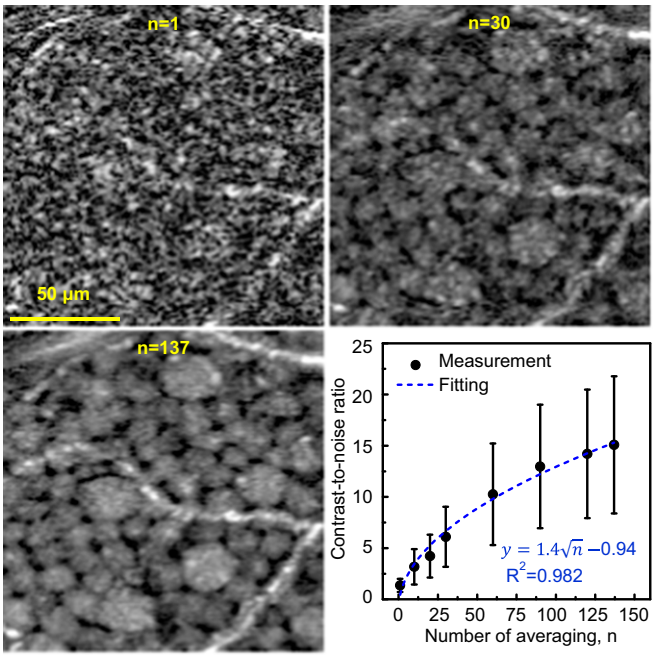

Fig. 1. Averaging registered AO-OCT images improves clarity of GCL somas. Magnified view of the same small patch of retina is shown with different amounts of averaging ($n = 1$, 30, and 137 images). Images are from 12–13.5° temporal to the fovea in subject S3. Plot shows the contrast-to-noise ratio (CNR) of 120 individual GCL somas computed as a function of images averaged (*Materials and Methods*). Error bars denote ±1 SD. CNR increase follows the square root of the number of images (dashed curve).

GCL Soma Size and Stack Thickness. We inspected the GCL of recorded retinal volumes to estimate the size and layering of GCL somas at different retinal eccentricities. Example images (Fig. 3 and Fig. S1) clearly reveal the retinal gradient of soma size for all four subjects. The high axial resolution of our AO-OCT enables visualization of the layering of GCL somas in depth, necessary for measurements of cell density and observations of the arrangement of somas in gaps between nerve fiber bundles and around blood vessels extending through the entire GCL (Figs. S2 and S3 and Movie S2). Stack thickness reached a maximum of 4–5 somas at 3–4.5° retinal eccentricity, decreasing rapidly toward the fovea and slowly away from it to a minimum thickness of 1. A thickness of ≥2 somas was observed up to 9.5° eccentric (Fig. S3). Note that counting the number of somas in stack required some judgment due to the varied spacing and size of the somas. Soma size is a distinguishing property of GCs related to their function and central projection (5, 6, 26). In our images, somas near the fovea are small and homogeneous, possibly due to packing constraints for achieving high visual acuity (26). In contrast, the patches 12–13.5° eccentric contain the largest and most varied sizes (5, 6, 26). Central tendency and variability of soma size are captured by the frequency distributions plotted in Fig. 4*A* and Fig. S4. For the four subjects, the distribution of soma diameter is 11.4 ± 1.8 μm (average ± SD) at 1.5–3° and 13.9 ± 3.1 μm at 12–13.5°, a 22% and 72% increase in size and variation.

A very small fraction of GCL cells (21 of 32,469 counted) at 1.5–3°, 3–4.5°, 6–7.5°, 8–9.5°, and 12–13.5° temporal to the fovea in the four subjects had giant somas (J cells), defined as a diameter greater than 26 μm (27). All but one of the giant somas were observed at the two largest retinal eccentricities, consistent with the reported distribution of giant cells whose frequency begins near this eccentricity range and peaks in the mid-peripheral retina (27). The largest had a diameter of 30.8 μm, almost exact in size to the 31-μm "giant" monkey GC Polyak used from his histology to illustrate this class (28).

GCL Soma Reflectance. We know of no reports on the reflectance properties of individual GCL somas. In this study, we discovered that larger somas are generally more reflective (amplitude/pixel measured at soma center) than the smaller ones, a significant difference ($P < 0.001$) in all subjects at all locations. This property is illustrated in the reflectance scatterplot in Fig. 4*C* that shows an average increase of 70% over the soma size range. Variation in reflectance must point to underlying differences in soma composition as measurements were made internal to somas that were selected from the same volume and narrow depth plane (14 μm). The latter avoided the influence of focus and other optical variations. Note that this approach parallels that commonly used to quantify reflectance variations of cone photoreceptors imaged with AO-flood, AO-SLO, and AO-OCT. Our measured variation in soma reflectance suggests a method for distinguishing GC subtypes based on soma composition. Reflectance may prove especially useful in studying central retina where GC subtype is difficult to establish based on soma size.

GC Soma Subtypes. From histology of excised tissue, it is known that parasol GCs generally exhibit larger somas than midget GCs (mGC), and this size difference increases with distance from the fovea (5, 29, 30). Our study confirms and extends that observation in living eyes by showing that the size distribution exhibits an increasingly positive skewness with retinal eccentricity (Pearson's

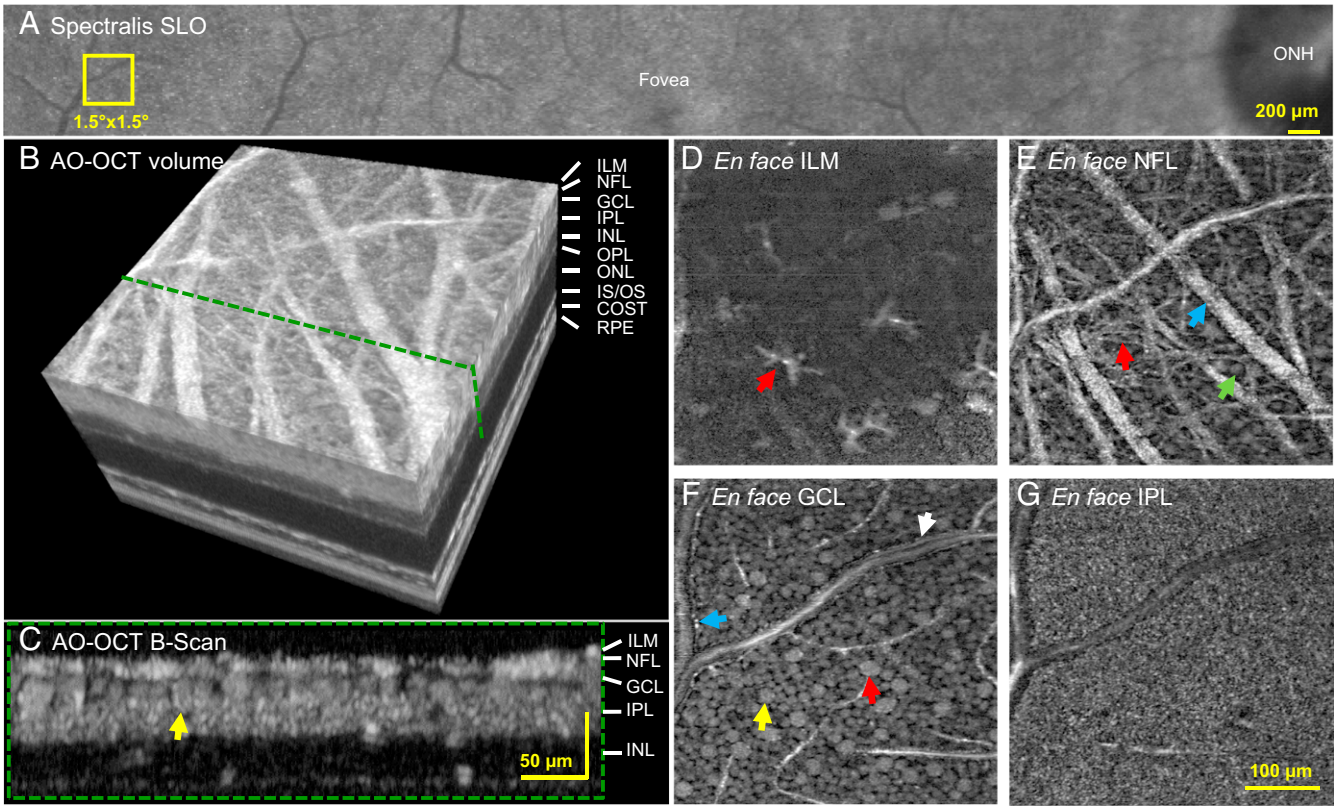

Fig. 2. Cellular structures of the inner layers of the retina using AO-OCT. (*A*) Yellow square at 12–13.5° temporal to the fovea in subject S3 denotes location imaged with AO-OCT. (*B*) Three-dimensional perspective of registered and averaged AO-OCT volume with green dashed line denoting cross-section of inner retina shown in *C*. Yellow arrow indicates same GCL soma in *C* and *F*. Images shown in *D*–*G* were extracted at depths of 0, 13, 22, and 46 µm below ILM. Scale bar in *G* also applies to *D*–*F*. (*D*) Surface of ILM. Bright, irregular star-like structures sparsely cover the surface of the ILM and are consistent in appearance with individual astrocyte or microglial cells. (*E*) A complex web of nerve fiber bundles of varying size disperse across the NFL. Some have a diameter as large as 30 µm (blue arrow), which compares to our previous AO-OCT observations (48). Others are as small as 3 µm, which matches the caliper of a single large GC axon. An arteriole/venule branches on the left. GCL somas appear between the overlying bundles near the image bottom (green arrow). (*F*) A mosaic of GCL somas of varying size tile the layer. Red arrow points to a large soma. Caliper of arteriole/venule in *E* is sufficiently large that it extends into the GCL. Note the distinct edges of the vessel walls (blue and white arrows) and the tight abutment of GCL somas. (*G*) The dense synaptic connections between axons of bipolar cells and dendrites of ganglion and amacrine cells present as a uniform mesh of high spatial frequency irregularities in the IPL. COST, cone outer segment tip; IS/OS, inner segment/outer segment junction; ONL, outer nuclear layer; OPL, outer plexiform layer (Movie S1).

moment coefficient increased from 0.53 to 1.45) and becomes bimodal for retinal eccentricities greater than 6°. To test whether these two modes represent the two primary subtypes of GCs in the macula (midget and parasol), we simultaneously fit two Gaussians to the bimodal distributions and subtracted the expected contribution of displaced amacrine cells (10) from the lower-diameter mode (*Materials and Methods*). When averaged across all subjects, the fractions of cells falling into the lower-diameter mode were 91%, 85%, and 86% for eccentricities of 6–7.5°, 8–9.5°, and 12–13.5°, respectively. These estimates fall between the fractional estimates of mGCs by Dacey (7) and Drasdo et al. (20) (Fig. S5), and the size distributions of our data fall within the range reported for midget and parasol somas in the human literature (Fig. 4*B*). We conclude from these observations that single-scatter imaging is capable of resolving and distinguishing the two primary subtypes of GCs that form parallel visual pathways through the optic nerve to visual centers of the brain (31) based on three fundamental soma features: size, density, and reflectance.

GC Soma Density. Histologic studies show that the spatial density of GC somas varies markedly across the retina—characterized by an elevated ring of densely packed, stacked somas surrounding the fovea—and across subjects (6, 7, 9, 10, 32–34). To determine the density in our subjects, we used soma counts (41,506) from 24 of 26 imaged locations and, as before, subtracted amacrine population estimates from the literature (10). Fig. 3 plot shows that the soma density distribution parallels that from histology, peaking at 3–4.5° with a sharp monotonic decrease toward the fovea and a gradual one away from it. Higher densities were found in nasal retina (S4), also consistent with histologic studies (10, 34). No significant difference was found for retinal eccentricities greater than 6° ($P = 0.11$–0.89). At lower retinal eccentricities, our peak densities were smaller than histologic estimates (10) with means and SDs of 19,162 ± 2,087 somas per mm^2 and 26,895 ± 4,899 somas per mm^2, respectively, a significant difference ($P = 0.011$). While part of this difference can be attributed to our coarse 1.5° × 1.5° sampling window, repeating the analysis using a smaller 0.17° × 0.1° window and a counting protocol consistent with that of Curcio and Allen (10) still yielded lower densities. We found no evidence of a scaling discrepancy nor that obstructions such as vasculature or other cellular structures within the GCL masked the underlying somas and caused undercounting. Somas were evident across the entire GCL thickness, and the 790-nm wavelength of our AO-OCT is minimally absorbed by retinal tissue. Thus, the discrepancy between our density results and those from histology remains an open question, compounded by the small sample sizes in both studies.

GC Projection onto Cone Photoreceptors. Single-scatter imaging with AO-OCT enables the measurement of physical parameters in the living human retina that are fundamental to the structure and function of GCs. As an example of elucidating GC function

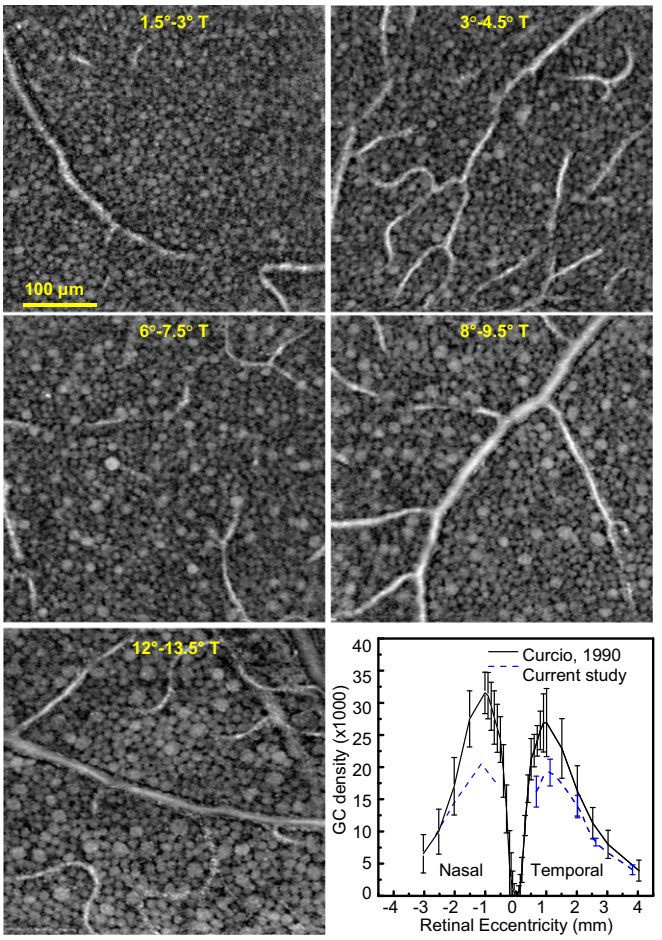

Fig. 3. *En face* images extracted from GCL at increasing retinal eccentricity of subject S4. A mosaic of GCL somas is observed at each eccentricity. (*Bottom Right*) GC soma density is plotted along the horizontal meridian of the macula. Retinal eccentricity is converted to millimeters to compare with histology data (10). AO-OCT temporal data are the average from four subjects and nasal is from S4. Error bars denote ±1 SD.

in retinal neural circuitry, we used our density measurements to derive individualized estimates of the pooling of cone signals by GC dendritic fields. Pooling of cone signals via intermediate bipolar cells is an anatomical necessity (because cones outnumber optic nerve fibers) that imposes fundamental limits on vision. mGCs in particular are important in determining visual acuity, yet histological estimates of the extent of their receptive fields and the number of mGCs that service each cone vary widely in the literature (20, 21). In the human fovea, the reported range of mGC-to-cone ratio is large (0.9–3.4), requiring profoundly different numbers of ON-center and OFF-center mGCs to encode the foveal image. To derive an estimate of this ratio from our in vivo AO-OCT data, we projected our measured GC coordinates onto our measured cone photoreceptor coordinates for the same subject. GC retinal eccentricity ranges of 1.5–3°, 3–4.5°, 6–7.5°, 8–9.5°, and 12–13.5° were estimated to project to cone retinal eccentricities of 0.35–1.2°, 1.2–2.6°, 4.5–6.5°, 7.1–8.9°, and 11.7–13.3° (21) (*Materials and Methods*). Cone densities in these eccentricity ranges (52,882, 34,178, 12,375, 9,728, and 6,602 cells per mm^2) were normal (35), with only one location (0.35–1.2°) statically lower ($P < 0.05$) than the histologic measurements of Curcio et al. (36). The average mGC-to-cone ratios at these cone locations were 1.60, 1.12, 0.98, 0.72, and 0.52. As shown in Fig. 4*D*, our ratio measurements are consistent with Watson's recent histology-based model (21), differing by 6%, 21%, 10%, 0.2%, and 4.1%, respectively. Our fovea ratio of 1.60 supports the view that the vertical pathway through the fovea connects two mGCs to one cone, allowing one to be ON center and the other OFF center (1). Individual differences, however, are notable with ratios across the four subjects varying by 9–70% [(max − min)/avg] depending on retinal location. This variation should affect visual resolution in these eyes as fundamental limits are imposed by the sampling of cone photoreceptors and mGCs (19). We can now test these limits by accounting for both.

Observing GCL Somas Under Thick NFL and at Foveal Rim. As shown in cross section and *en face* of Fig. S6 (also see Movie S3), the NFL at 8–9.5° nasal (50 µm thick) approaches the thickest in the macula (37). It densely covers the entire volume image, and its peak amplitude reflectance is 6.5 times greater than that of the underlying GCL somas, a difference that is best appreciated by the cross-sectional image displayed in the figure on a linear, as opposed to logarithmic, scale. Despite this thick, brightly reflecting layer that lies immediately above the somas, the soma mosaic can be extracted as evident in the *en face* GCL image in the same figure.

In contrast, close to the foveal center where the NFL is absent, the 0.35–1.85° retinal patch of S1 (Fig. S7 and Movie S4) reveals that GCL somas extend all of the way to the foveal rim of the GCL where they abut the ILM. Presumably, these somas are most critical for visual acuity as they are thought to project to photoreceptors at the foveal center. Prominent in the *en face* image is the extension of the soma mosaic into the foveal avascular zone, defined by the innermost ring of retinal capillaries encircling the fovea. In both subjects imaged at this location (S1 and S4), GCL somas did not extend more than 100 µm, consistent with the general rule for mammals that metabolically active cells should not be more than this distance to preserve molecular exchange via

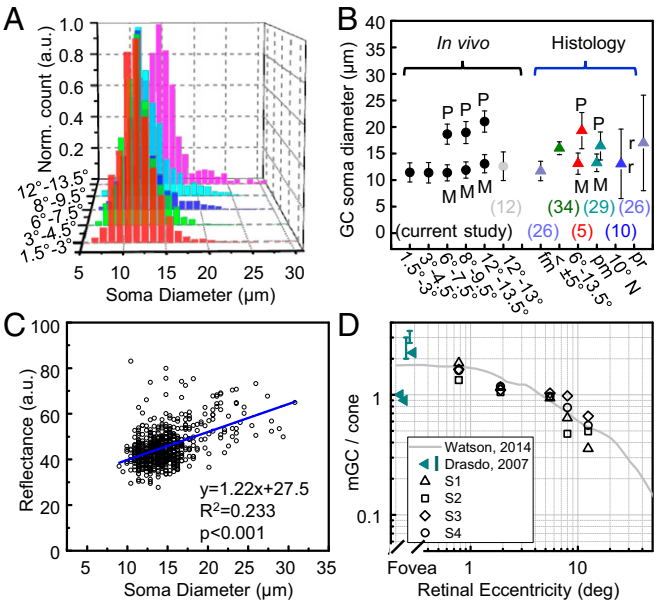

Fig. 4. Properties of soma size, reflectance, and pooling of cone signals. (*A*) Representative GCL soma size distribution (S4) is color coded by retinal eccentricity. (*B*) Average GC soma diameter obtained by Gaussian fits to the four subjects in temporal retina with measurements reported in the literature for humans (5, 10, 12, 26, 29, 34). Error bars denote ±1 SD unless labeled with an *r* to denote minimum-to-maximum range. M and P denote midget and parasol cells. Labels along *x* axis report retinal location of measurement. fm, foveal margin; pm, papillomacular; pr, peripheral retina. (*C*) Representative reflectance of 637 GCL somas at 12–13.5° temporal to the fovea in subject S4. Blue line shows linear regression curve. (*D*) mRGC-to-cone ratio for four subjects is plotted with Watson's histology-based model for humans (figure 14 of ref. 21) and fovea ratios in table 1 of Drasdo et al. (20).

diffusion (1). This suggests that capillary dropout along the innermost ring, as for example occurs in diabetic retinopathy (38), is likely detrimental to these critical GCs, which we can now monitor in these patients as the disease progresses.

Visualizing GCs and Other Neurons Across the Retina. While our study was confined to the horizontal meridian of the macula, our measurements have broader significance given the common neural layering of the retina across the posterior pole and radial symmetry of the macula about the fovea. Given these commonalities, our method should allow observation of GCL somas anywhere in the macula and beyond, whether stacked on each other (Figs. S2 and S3 and Movie S2), lying beneath a thick and highly scattering NFL (Fig. S6 and Movie S3), or aggregated at the foveal rim where the smallest and closest-packed GCL somas are found (Fig. S7 and Movie S4). Although we emphasized GCL somas in this report, our images also provide detailed views of nerve fiber bundles and GC axons that form them. An exemplary example is Movie S5, which shows several fiber bundles dissolving into an intricate labyrinth of axons. In general, our AO-OCT method holds promise for visualizing cells across all retinal layers and, thus, exposing the anatomical substrate for neural processing of visual information. Fig. 5 illustrates this capability, showing cells extracted from different depths [NFL to retinal pigment epithelium (RPE)] in the same retinal patch. In these images, we can discern the types and densities of cells that compose each layer. Interestingly, the inner nuclear layer (INL) image depicts a fine mesh of tightly packed, small (5-μm diameter), faint structures suggestive of bipolar somas (9) and sparse, large (18-μm diameter), bright structures suggestive of displaced GC somas (39). These await further study.

By imaging tens of thousands of GCL somas in four subjects, we have demonstrated a path for visualizing and quantifying these elusive cells as well as other transparent neurons and cellular structures in the living human retina. While application of this method to diseased eyes is apparent, there is also optimism that the methodology can be improved further, for example, to characterize the dendritic morphology and soma organelle pattern that are more definitive cues of retinal cell type. Such characterization might be possible using the complex field recorded by AO-OCT (e.g., ref. 40) to map the physiological dynamics of these cellular compartments. For now, our images are generating more questions than answers, reminiscent of what some of us experienced two decades ago with the first photoreceptor images (41).

Materials and Methods

Subjects. Four subjects, ranging in age from 24 to 50 y (S1 = 24, S2 = 26, S3 = 47, and S4 = 50 y old) and free of ocular disease, participated in the experiments. All subjects had best corrected visual acuity of 20/20 or better and a spherical equivalent refraction between 0 and −2.5 diopters. All had normal intraocular pressure (IOP), performance on perimetry, and appearance of optic disk and fundus, as determined by the Indiana University School of Optometry clinic. The one exception was S4 who had a history of elevated IOP (range 20–22), but normal otherwise. Eye lengths ranged from 23.27 to 25.40 mm as measured with the IOLMaster (Zeiss), and were used to scale the retinal images from degrees to millimeters (42). All procedures on the subjects adhered to the tenets of the Declaration of Helsinki and were approved by the Institutional Review Board of Indiana University. Written consent was obtained after the nature and possible risks of the study were explained.

Experimental Design. The subject's eye was cyclopleged and dilated with tropicamide 0.5%. The eye and head were aligned and stabilized using a bite bar mounted to a motorized XYZ translation stage. Images were acquired with the Indiana AO-OCT system (43, 44) with system focus placed precisely at the GCL to maximize sharpness of GCL somas. Correct placement was realized by optimizing brightness of the GCL using the real-time displayed B-scan (cross sectional) images and sharpness of the NFL vasculature in the *en face* images. AO-OCT volumes were acquired on the subjects at 10 macular locations along the horizontal meridian that bisected the fovea. The five locations (1.5–3°, 3–4.5°, 6–7.5°, 8–9.5°, and 12–13.5°) temporal to the fovea were imaged in four subjects and the four (1.5–3°, 3–4.5°, 6–7.5°, and 8–9.5°) nasal to it were imaged in one. An extreme foveal location at 0.35–1.85° temporal was imaged in two subjects. For each retinal location, 10–15 AO-OCT videos (each ∼4 s in duration) were acquired over ∼10 min. Each video consisted of 11 volumes. The volumes covered a 1.5° × 1.5° field of view of the retina, and A-scans were sampled at 1 μm per pixel in both lateral dimensions. Fast A-scan and B-scan rates of 500 KHz and 1.1 KHz reduced, but did not eliminate, eye motion artifacts.

Images were also acquired of other retinal cells by focusing the system to the desired depth that maximized cell sharpness. This included imaging cone photoreceptors along the horizontal meridian that projected to the GCs at 1.5–3°, 3–4.5°, 6–7.5°, 8–9.5°, and 12–13.5°. Commercial (Spectralis; Heidelberg Engineering) spectral-domain OCT and SLO images were acquired on all subjects and covered the retinal locations imaged with AO-OCT.

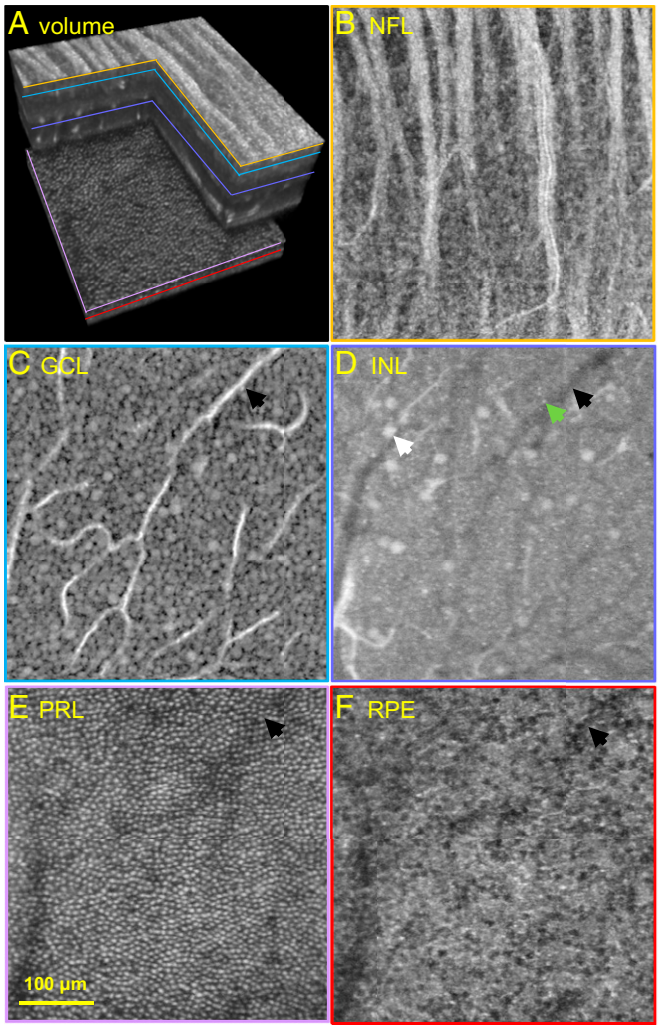

Fig. 5. Cells at different depths in the same retinal patch of subject S4 as visualized with AO-OCT. (*A*) Three-dimensional perspective of registered and averaged AO-OCT volume with colored lines denoting retinal depths at which the *en face* images in *B–F* were extracted. Images depicting individual NF bundles (*B*), GCL somas (19,162 cells per mm^2) (*C*), suggestive somas of bipolar (green arrow) and displaced GCs (white arrow) near the IPL interface (*D*), cone photoreceptors (16,341 cells per mm^2) (*E*), and RPE cells (4,893 cells per mm^2) (*F*). Black arrows in *C–F* indicate the same blood vessel and its shadow. The *en face* images were extracted from volumes acquired at 3–4.5° retinal eccentricity with system focus shifted axially to maximize sharpness of the cell layer of interest.

Postprocessing of AO-OCT Volumes. Volumes were reconstructed; dewarped to correct nonlinearities in the fast-axis scan pattern; registered in three dimensions to correct eye motion artifacts; and averaged to increase signal to noise. Images of GCL somas are difficult to register with conventional 2D strip-wise registration methods (15, 45) owing to the high translucency of these cells. We overcame this obstacle by using a custom 3D strip-wise registration algorithm (46) that operates on individual fast B-scans, thus using all available information in the

volumes and precluding the need of a GC signal. The registered and averaged volumes were used for all further analyses. Displayed volumes are shown as log intensity following the OCT literature, unless specified otherwise.

Quantifying Soma Size and Size Distribution. The diameter of each GCL soma was computed based on an *en face* (XY) view of the soma and the 3D coordinates of its center using software developed in MATLAB. The *en face* view was a three-pixel (2.82 μm) projection in depth of the reflectance distribution around the soma center. A circumferential average about the soma center in the *en face* view resulted in a 1D reflectance trace. Cell diameter was defined as twice the distance between the cell center and the minimum in the reflectance trace.

For each subject and retinal eccentricity, a single Gaussian function was fit to the soma size distribution where it appeared unimodal (for retinal locations up to 6°) and two Gaussian functions where it appeared bimodal (for retinal locations at and greater than 6°). The Gaussian fits were used to quantify the peak and range of soma diameter and the fraction of each mode.

Quantifying Soma Density. GCL soma centers were projected onto an *en face* plane from which soma densities were determined by two different methods. The first used Voronoi mapping of the soma mosaic, a mathematical construct widely used for quantifying cell association in retina tissue (47). For this method, soma density was defined as the ratio of total number of Voronoi cells to total area of the Voronoi cells. This approach avoided edge effects of the $1.5° \times 1.5°$ imaging window and blood vessels that can generate errors in the density count. The second method followed traditional histologic approaches. Specifically, cell centers were counted that fell within a small $0.17° \times 0.1°$ sampling window free of vasculature. The window size, number of windows, and counting protocol followed that of Curcio et al. (10), except we relied on cell centers as opposed to nucleolus locations, which we could not detect in our images.

We did not distinguish GCs from displaced amacrine cells, which represent 1–22% of the soma population in the GCL from central fovea to 13.5° (10). To facilitate comparison, we used displaced amacrine population values from the literature (10) to offset our count.

Determine mGC-to-Cone Ratio. We projected the GC coordinates measured with AO-OCT onto the cone photoreceptor coordinates, also measured with AO-OCT, by applying the displacement function given by equation 5 of Watson (21) for the horizontal meridian. This function accounts for the lateral displacement of GCs, which can exceed 600 μm (~2°) depending on retinal eccentricity and is caused by the lateral extension of photoreceptor axons and connections of the bipolar cells. Our projection took into account annular scaling between the GC and cone layers, and was adjusted for the proportion of GCs that are midget. For GCs at retinal eccentricities of 6–7.5°, 8–9.5°, and 12–13.5° where the GC size distribution was bimodal, we used the lower-diameter mode to estimate the mGC fraction. Nearer to the fovea where bimodality was not observed, we used the fractional estimate (89.3%) by Drasdo et al. (20).

ACKNOWLEDGMENTS. We thank Matt Lang, Omer Kocaoglu, Ayoub Lassoued, Nhan Do, and Tim Turner for technical assistance and Xiaofeng Qi, Larry Thibos, and James Crowell for edits to the manuscript. This study was supported by NIH Grants EY018339 and EY019008 and by the Indiana University Collaborative Research Grant fund of the Office of the Vice President for Research.

1. Rodieck RW (1998) *The First Steps in Seeing* (Sinauer Associates, Sunderland, MA).
2. Williams DR (2011) Imaging single cells in the living retina. *Vision Res* 51:1379–1396.
3. Balendra SI, Normando EM, Bloom PA, Cordeiro MF (2015) Advances in retinal ganglion cell imaging. *Eye (Lond)* 29:1260–1269.
4. Werkmeister RM, Cherecheanu AP, Garhofer G, Schmidl D, Schmetterer L (2013) Imaging of retinal ganglion cells in glaucoma: Pitfalls and challenges. *Cell Tissue Res* 353:261–268.
5. Rodieck RW, Binmoeller KF, Dineen J (1985) Parasol and midget ganglion cells of the human retina. *J Comp Neurol* 233:115–132.
6. Quigley HA, Dunkelberger GR, Green WR (1989) Retinal ganglion cell atrophy correlated with automated perimetry in human eyes with glaucoma. *Am J Ophthalmol* 107:453–464.
7. Dacey DM (1993) The mosaic of midget ganglion cells in the human retina. *J Neurosci* 13:5334–5355.
8. Gualda EJ, Bueno JM, Artal P (2010) Wavefront optimized nonlinear microscopy of ex vivo human retinas. *J Biomed Opt* 15:026007.
9. Lei Y, et al. (2011) Transretinal degeneration in ageing human retina: A multiphoton microscopy analysis. *Br J Ophthalmol* 95:727–730.
10. Curcio CA, Allen KA (1990) Topography of ganglion cells in human retina. *J Comp Neurol* 300:5–25.
11. Grieve K, Thouvenin O, Sengupta A, Borderie VM, Paques M (2016) Appearance of the retina with full-field optical coherence tomography. *Invest Ophthalmol Vis Sci* 57:OCT96–OCT104.
12. Rossi EA, et al. (2017) Imaging individual neurons in the retinal ganglion cell layer of the living eye. *Proc Natl Acad Sci USA* 114:586–591.
13. Price DA, Swanson WH, Horner DG (2017) Using perimetric data to estimate ganglion cell loss for detecting progression of glaucoma: A comparison of models. *Ophthalmic Physiol Opt* 37:409–419.
14. Cordeiro MF, et al. (2017) Real-time imaging of single neuronal cell apoptosis in patients with glaucoma. *Brain* 140:1757–1767.
15. Jonnal RS, et al. (2016) A review of adaptive optics optical coherence tomography: Technical advances, scientific applications, and the future. *Invest Ophthalmol Vis Sci* 57:OCT51–OCT68.
16. Liu Z, Kocaoglu OP, Miller DT (2016) 3D imaging of retinal pigment epithelial cells in the living human retina. *Invest Ophthalmol Vis Sci* 57:OCT533–OCT543.
17. Liu Z, Kurokawa K, Zhang F, Miller DT (2017) Characterizing motility dynamics in human RPE cells. *Opthalmic Technologies XXVII*, 10045:1004515.
18. Wilkinson MO, Anderson RS, Bradley A, Thibos LN (2016) Neural bandwidth of veridical perception across the visual field. *J Vis* 16:1–17.
19. Rossi EA, Roorda A (2010) The relationship between visual resolution and cone spacing in the human fovea. *Nat Neurosci* 13:156–157.
20. Drasdo N, Millican CL, Katholi CR, Curcio CA (2007) The length of Henle fibers in the human retina and a model of ganglion receptive field density in the visual field. *Vision Res* 47:2901–2911.
21. Watson AB (2014) A formula for human retinal ganglion cell receptive field density as a function of visual field location. *J Vis* 14:1–17.
22. Quigley HA (1999) Neuronal death in glaucoma. *Prog Retin Eye Res* 18:39–57.
23. Sena DF, Lindsley K (2017) Neuroprotection for treatment of glaucoma in adults. *Cochrane Database Syst Rev* 2017:CD006539.
24. Galetta KM, Calabresi PA, Frohman EM, Balcer LJ (2011) Optical coherence tomography (OCT): Imaging the visual pathway as a model for neurodegeneration. *Neurotherapeutics* 8:117–132.
25. Goodman JW (2007) *Speckle Phenomena in Optics Theory and Applications* (Roberts and Company, Greenwood Village, CO), pp 25–58.
26. Stone J, Johnston E (1981) The topography of primate retina: A study of the human, bushbaby, and new- and old-world monkeys. *J Comp Neurol* 196:205–223.
27. Dawson WW, Hawthorne MN, Parmer R, Hope GM, Hueter R (1989) Very large neurons of the inner retina of humans and other mammals. *Retina* 9:69–74.
28. Polyak SL (1941) *The Retina* (Univ of Chicago Press, Chicago).
29. Pavlidis M, Stupp T, Hummeke M, Thanos S (2006) Morphometric examination of human and monkey retinal ganglion cells within the papillomacular area. *Retina* 26:445–453.
30. Watanabe M, Rodieck RW (1989) Parasol and midget ganglion cells of the primate retina. *J Comp Neurol* 289:434–454.
31. Lennie P, Trevarthen CB, Van Essen D, Wässle H (1990) Parallel processing of visual information. *Visual Perception. The Neurophysiological Foundations*, eds Spillmann L, Werner JS (Academic, New York), pp 103–128.
32. Gao H, Hollyfield JG (1992) Aging of the human retina. Differential loss of neurons and retinal pigment epithelial cells. *Invest Ophthalmol Vis Sci* 33:1–17.
33. Curcio CA, Drucker DN (1993) Retinal ganglion cells in Alzheimer's disease and aging. *Ann Neurol* 33:248–257.
34. Blanks JC, Torigoe Y, Hinton DR, Blanks RH (1996) Retinal pathology in Alzheimer's disease. I. Ganglion cell loss in foveal/parafoveal retina. *Neurobiol Aging* 17:377–384.
35. Song H, Chui TYP, Zhong Z, Elsner AE, Burns SA (2011) Variation of cone photoreceptor packing density with retinal eccentricity and age. *Invest Ophthalmol Vis Sci* 52:7376–7384.
36. Curcio CA, Sloan KR, Kalina RE, Hendrickson AE (1990) Human photoreceptor topography. *J Comp Neurol* 292:497–523.
37. Hood DC, et al. (2012) The nature of macular damage in glaucoma as revealed by averaging optical coherence tomography data. *Transl Vis Sci Technol* 1:3.
38. Agemy SA, et al. (2015) Retinal vascular perfusion density mapping using optical coherence tomography angiography in normals and diabetic retinopathy patients. *Retina* 35:2353–2363.
39. Liao HW, et al. (2016) Melanopsin-expressing ganglion cells on macaque and human retinas form two morphologically distinct populations. *J Comp Neurol* 524:2845–2872.
40. Kurokawa K, Liu Z, Miller DT (2017) Adaptive optics optical coherence tomography angiography for morphometric analysis of choriocapillaris [Invited]. *Biomed Opt Express* 8:1803–1822.
41. Miller DT, Williams DR, Morris GM, Liang J (1996) Images of cone photoreceptors in the living human eye. *Vision Res* 36:1067–1079.
42. Bennett AG, Rudnicka AR, Edgar DF (1994) Improvements on Littmann's method of determining the size of retinal features by fundus photography. *Graefes Arch Clin Exp Ophthalmol* 232:361–367.
43. Liu Z, Kocaoglu OP, Miller DT (2013) In-the-plane design of an off-axis ophthalmic adaptive optics system using toroidal mirrors. *Biomed Opt Express* 4:3007–3029.
44. Kocaoglu OP, Turner TL, Liu Z, Miller DT (2014) Adaptive optics optical coherence tomography at 1 MHz. *Biomed Opt Express* 5:4186–4200.
45. Jonnal RS, Kocaoglu OP, Wang Q, Lee S, Miller DT (2012) Phase-sensitive imaging of the outer retina using optical coherence tomography and adaptive optics. *Biomed Opt Express* 3:104–124.
46. Do NH (2016) Parallel processing for adaptive optics optical coherence tomography (AO-OCT) image registration using GPU. Master's thesis (Indiana University–Purdue University Indianapolis, Indianapolis, IN).
47. Morgan JI, Dubra A, Wolfe R, Merigan WH, Williams DR (2009) In vivo autofluorescence imaging of the human and macaque retinal pigment epithelial cell mosaic. *Invest Ophthalmol Vis Sci* 50:1350–1359.
48. Kocaoglu OP, et al. (2011) Imaging retinal nerve fiber bundles using optical coherence tomography with adaptive optics. *Vision Res* 51:1835–1844.
49. ANSI Z136.1 (2014) *American National Standard for Safe Use of Lasers* (Laser Institute of America, Orlando, FL).